Biosensors and Bioelectronics 260 (2024) 116446



Contents lists available at ScienceDirect

Biosensors and Bioelectronics

journal homepage: www.elsevier.com/locate/bios





Monolayer, open-mesh, pristine PEDOT:PSS-based conformal brain implants for fully MRI-compatible neural interfaces

Jung-Hoon Hong ^{a,1}, Ju Young Lee ^{a,1}, Ankan Dutta ^{b,c,1}, Sol Lip Yoon ^d, Young Uk Cho ^{a,e}, Kyubeen Kim ^a, Kyowon Kang ^a, Hyun Woo Kim ^a, Dae-Hee Kim ^f, Jaejin Park ^a, Myeongki Cho ^a, Kiho Kim ^a, Jong Bin An ^g, Hye-Lan Lee ^d, Dosik Hwang ^h, Hyun Jae Kim ^g, Yoon Ha ^{d,i}, Hye Yeong Lee ^{d,***}, Huanyu Cheng ^{b,c,**}, Ki Jun Yu ^{a,j,*}

- ^a Functional Bio-integrated Electronics and Energy Management Lab, School of Electrical and Electronic Engineering, Yonsei University, 50 Yonsei-ro, Seodaemun-gu, 03722, Seoul, Republic of Korea
- b Department of Engineering Science and Mechanics, The Pennsylvania State University, University Park, 16802, State College, PA, USA
- ^c Center for Neural Engineering, The Pennsylvania State University, University Park, 16802, State College, PA, USA
- d Spine & Spinal Cord Institute, Department of Neurosurgery, College of Medicine, Yonsei University, 03722, Seoul, Republic of Korea
- e Center for Emergent Matter Science (CEMS), RIKEN, The Institute of Physical and Chemical Research, 351-0198, Saitama, Japan
- f Avison Biomedical Research Center, College of Medicine, Yonsei University, 50-1 Yonsei-ro, Seodaemun-gu, 03722, Seoul, Republic of Korea
- g Electronic Device Laboratory, School of Electrical and Electronic Engineering, Yonsei University, 50 Yonsei-ro, Seodaemun-gu, 03722, Seoul, Republic of Korea
- ^h School of Electrical and Electronic Engineering, Yonsei University, 50 Yonsei-ro, Seodaemun-gu, 03722, Seoul, Republic of Korea
- i POSTECH Biotech Center, Pohang University of Science and Technology (POSTECH), 37673, Pohang, Republic of Korea
- ^j Department of Electrical and Electronic Engineering, YU-Korea Institute of Science and Technology (KIST) Institute, Yonsei University, 50, Yonsei-ro, Seodaemun-gu, 03722, Seoul, Republic of Korea

ARTICLE INFO

Keywords:
Neural implant
Magnetic resonance imaging
MRI-compatible neural interface
PEDOT:PSS
Open-mesh structure

ABSTRACT

Understanding brain function is essential for advancing our comprehension of human cognition, behavior, and neurological disorders. Magnetic resonance imaging (MRI) stands out as a powerful tool for exploring brain function, providing detailed insights into its structure and physiology. Combining MRI technology with electrophysiological recording system can enhance the comprehension of brain functionality through synergistic effects. However, the integration of neural implants with MRI technology presents challenges because of its strong electromagnetic (EM) energy during MRI scans. Therefore, MRI-compatible neural implants should facilitate detailed investigation of neural activities and brain functions in real-time in high resolution, without compromising patient safety and imaging quality. Here, we introduce the fully MRI-compatible monolayer openmesh pristine PEDOT:PSS neural interface. This approach addresses the challenges encountered while using traditional metal-based electrodes in the MRI environment such as induced heat or imaging artifacts. PEDOT:PSS has a diamagnetic property with low electrical conductivity and negative magnetic susceptibility similar to human tissues. Furthermore, by adopting the optimized open-mesh structure, the induced currents generated by EM energy are significantly diminished, leading to optimized MRI compatibility. Through simulations and experiments, our PEDOT:PSS-based open-mesh electrodes showed improved performance in reducing heat generation and eliminating imaging artifacts in an MRI environment. The electrophysiological recording capability was also validated by measuring the local field potential (LFP) from the somatosensory cortex with an in vivo experiment. The development of neural implants with maximized MRI compatibility indicates the possibility of potential tools for future neural diagnostics.

^{*} Corresponding author. Functional Bio-integrated Electronics and Energy Management Lab, School of Electrical and Electronic Engineering, Yonsei University, 50 Yonsei-ro, Seodaemun-gu, 03722, Seoul, Republic of Korea.

^{**} Corresponding author. Department of Engineering Science and Mechanics, The Pennsylvania State University, University Park, State College, 16802, PA, USA.

*** Corresponding author. Spine & Spinal Cord Institute, Department of Neurosurgery, College of Medicine, Yonsei University, 03722, Seoul, Republic of Korea.

 $[\]textit{E-mail addresses: } \underline{kimura416@yuhs.ac} \ (H.Y. Lee), \underline{huanyu.cheng@psu.edu} \ (H. Cheng), \underline{kijunyu@yonsei.ac.kr} \ (K.J. Yu).$ $^{1} \ These \ authors \ contributed \ equally \ to \ this \ work.$

1. Introduction

The human brain, composed of billions of neurons, serves as the central organ for most vital activities such as cognition and human behavior (Chen et al., 2017; Cho et al., 2022b; Luan et al., 2020). In the pursuit of extending the human health span, research on neural implants has been vigorously conducted to facilitate neurological diagnostics and treatments (Kang et al., 2024; Park et al., 2023; Shabani et al., 2023). Recent endeavors in brain-machine interface research, exemplified by Neuralink, have highlighted the importance of performance and stability in neural implants as these efforts aim to understand and communicate directly with this complex organ (Shen et al., 2023; Tang et al., 2023). Using electrodes for neural interfacing, which measures electrophysiological signals, facilitates the direct measurement of electrical signals evoked by neuronal signal transmission (Cho et al., 2024a; Lee et al., 2022). While electrophysiological recordings exhibit high temporal resolution, their spatial resolution is limited because of electrophysiological recording obtain signals from specific areas around the recording electrodes (Cho et al., 2021). Given the complexity of neural activity in the brain, it is necessary to measure high-quality, localized signals for a comprehensive understanding of the brain; furthermore, it is crucial to link these measurements with physiological changes across broader regions (Cho et al., 2024b).

Magnetic resonance imaging (MRI) is a powerful medical imaging technique that can provide comprehensive structural data and physiological information about the brain (Zhang et al., 2021). Furthermore, functional sequences, such as functional magnetic resonance imaging (fMRI), are actively researched because they noninvasively show physiological changes in the body, such as blood flow within the brain, through images. Therefore, integrating MRI technology, which allows for high spatial resolution monitoring of physiological changes, with neural interfaces, which offer electrophysiological measurements at high temporal resolution, is of significant importance. This combination enables synergistic acquisition of physiological data that exhibits high spatiotemporal resolutions (Zhao et al., 2020). Despite these significant benefits, there are difficulties in applying conventional neural implants alongside MRI technology because of compatibility issues between the MRI environment and the neural interface (Erhardt et al., 2018; Zrinzo et al., 2011). MRI uses a strong static magnetic field along with high-powered electromagnetic (EM) energy. Such an electromagnetically intense MRI environment poses two major compatibility issues with conventional neural implants (Sayed et al., 2020).

First, a potential for medical image distortion exists. Most conventional biocompatible metal-based electrodes exhibit a significant difference in magnetic susceptibility compared to the surrounding soft brain tissue. This susceptibility mismatch leads contamination of medical imaging results, which is also called image artifacts (Starčuková et al., 2008; Zhang et al., 2021). Additionally, the strong EM forces within the MRI can induce EM fields near the neural interface, further impacting imaging outcomes adversely. Second, a potential concern arises regarding tissue damage attributable to heating around the neural interface. This heating can be due to the heating of the electrodes themselves in the strong EM field, or it can result from flows of induced currents into surrounding tissues which are generated in conductive neural implants (Foster and Glaser, 2007; Graf et al., 2007). In the case of the brain, which is the central organ for vital activities, it is imperative to minimize brain tissue damage caused by heating because of difficulty in regenerating damaged neurons (Binan et al., 2014; Collins et al., 2022). In these contexts, the development of MRI-compatible electrophysiological neural interfaces is a critical challenge and is currently the subject of active research.

To develop MRI-compatible neural implants, both obtaining a clear MRI image and safety of the patient must be considered. To meet these requirements, attention is necessary to both material properties and structural form of neural implants. In an MRI environment, the heating induced by radio frequency (RF) energy is significantly influenced by the

specific absorption rate (SAR), which is expressed as follows:

$$SAR = \int \frac{\sigma|\mathbf{E}|^2}{2\rho} dV \tag{Eq. 1}$$

where σ denotes the electrical conductivity of the tissue, ρ represents the mass density of the tissue, and E refers to the electrical field generated by the RF coil. The SAR represents the amount of RF energy absorbed by a patient in an environment where a device is implanted (Chou et al., 1996; Muranaka et al., 2007). Therefore, this rate of RF energy absorption, which is also related to the electrical conductivity of the material, is closely associated with the generation of heat by implants in the MRI environment (Bhargava et al., 2020). High-conductivity materials such as Pt, undergo substantial RF-induced heating during MRI scanning. Consequently, tissues surrounding metal-based neural implants can be exposed to high SAR, potentially causing biological tissue damage due to heat induced from neural implants (Davis et al., 1981). Moreover, the magnetic susceptibility of a material, a physical property indicating its response to a magnetic field, is a crucial factor in MRI (Starčuková et al., 2008). Materials with high magnetic susceptibility strongly react to the magnetic fields from the MRI, leading to field imbalances and MRI artifacts. To minimize interference during MRI scans. the implant material should have a magnetic susceptibility similar to human tissue, which typically ranges from -11 to -7 ppm in volume susceptibility (Zhang et al., 2021).

Traditional metal-based neural implants, such as those made of Pt, have limitations in MRI environments owing to their high conductivity and magnetic susceptibility. Such implants can compromise patient safety and image quality (Thelen et al., 2006; Zhang et al., 2021). To solve this issue, an MRI-compatible neural implant was developed in the form of fiber by combining graphene and Cu which has magnetic susceptibility similar to that of human tissue (Zhao et al., 2016). However, despite their similar magnetic susceptibilities with tissue, materials like Cu, which have high electrical conductivity, are still rendered unsuitable because RF energy absorption causes tissue heating. Additionally, fiber implants have shown limitations regarding spatial resolution, therefore, multisite recording is not possible. This problem impedes covering large areas or precise recordings at various depths within cortical layers (Chuapoco et al., 2019).

Recently, materials like poly (3,4-ethylenedioxythiophene) polystyrene sulfonate (PEDOT:PSS) have gained attention because of their potential as MRI-compatible neural implants. PEDOT:PSS has a lower electrical conductivity than conventional metal electrodes. However, when used for neural signal recording implants, PEDOT:PSS is suitable for neural signal recording due to its large surface area, leading to lower electrochemical impedance (Cho et al., 2022a). Furthermore, PEDOT: PSS has low magnetic susceptibility, which makes it compatible with MRI environments (Cho et al., 2024b). Many studies on MRI-compatible neural implants have adopted materials or structures that are challenging for micropatterning processes (Lu et al., 2019; Zhao et al., 2020). In contrast, the micropatterning capability of PEDOT:PSS enables fabrication of customized electrodes tailored to specific requirements, allowing for precise electrode placement in wide areas (Cho et al., 2022a).

Beyond material differences, structural modifications of electrodes also influence currents induced because of strong EM energy. According to Faraday's law, the magnitude of total induced voltage in an EM field environment can be expressed as follows:

$$\varphi = -\iint \frac{\partial \overrightarrow{B}}{\partial t} \bullet \overrightarrow{dA}$$
 (Eq. 2)

where \overrightarrow{B} is the magnetic field and \overrightarrow{A} is the bounded surface by a closed contour. When the conductor forms a closed loop, the effective area influenced by the EM field exceeds the actual surface area of the conductor. Consequently, in an RF environment, the formation of a

closed loop induces a higher voltage and current than those based on the actual area. This phenomenon can lead to intense internal heating of the electrode and potentially cause damage to surrounding tissues (Nyenhuis et al., 2005). Furthermore, the currents induced by the electrode can adversely impact imaging outcomes due to the generation of a secondary magnetic field (Ahn and Cho, 1991). This additional magnetic field can result in further magnetic field imperfections, resulting in undesirable distortions in MRI scans. To overcome these challenges, open-mesh structures that avoid closed loops formation were proposed as MRI-compatible designs (Fan et al., 2014; Tian et al., 2019). Compared to other electrode structures, an open-mesh electrode effectively diminishes the area enclosed by a closed contour. According to Faraday's law, this reduction of the closed loop area through modifications in electrode structure results in decreased induced voltage and currents. This effect reduces internal heating within the conductor and improves the quality of MRI images. In summary, by combining material MRI compatibility with structural considerations, a MRI-compatible neural interface can be developed, minimizing the problems associated with MRI scanning.

Here, we introduce a fully MRI-compatible monolayer open-mesh pristine PEDOT:PSS neural interface, which has been specifically designed to maximize MRI compatibility through both material and structural optimizations. PEDOT:PSS is a conductive diamagnetic polymer material known for its high MRI compatibility. This material can achieve excellent electrode impedance suitable for neural signal measurements through post-treatment processes such as ethylene glycol (EG) treatment. Using photolithography-based micropatterning technology of PEDOT:PSS with a line width of 10 μm , we have developed electrodes for neural probes with an open-mesh structure that minimizes induced currents. Through this, we have successfully developed a neural probe that is not only materially superior but also structurally optimized for MRI compatibility.

In this study, we first conducted simulations to compare heat generation and extent of image artifacts among various structures of PEDOT:PSS electrodes. Electrodes with an open-mesh structure exhibited superior performance in minimizing heat generation and imaging artifacts compared to those with square or closed-mesh structures. We confirmed that electrodes with an open-mesh structure exhibited superior performance in terms of both heat generation and imaging artifacts compared to those with square or closed-mesh structures. Furthermore, we proposed an optimized open-mesh structured electrodes based on our mesh structure optimization theory. MRI was conducted for Pt and PEDOT:PSS electrodes with various structures to observe artifact-free characteristics during MRI scans. Additionally, to assess the difference in electrode heating under strong EM fields, RF heating tests and in-MRI temperature measurement experiments were conducted, experimentally verifying the lower heat generation of open-mesh electrodes. The performance of the MRI-compatible electrodes as a neural interface was evaluated by inserting them into the somatosensory cortex (S1) of rats and measuring their local field potential (LFP). When the hind-paws of the rats were electrically stimulated, changes in electrophysiological signals in S1 were observed, and the capability of the multichannel neural probes was confirmed by variations in signal strength with changes in the measurement depth.

2. Material and methods

2.1. Fabrication process of fully MRI-compatible open-mesh PEDOT:PSS neural interface

Polydimethylsiloxane (PDMS, Dow Corning) with a ratio of 17:1 was spin-coated onto a glass substrate at a speed of 3000 rpm and baked on a hot plate at 90 $^{\circ}$ C for 30 min and then 110 $^{\circ}$ C for 2 h. Subsequently, a Polyethylene terephthalate (PET) substrate (thickness, 25 μm , GFM Korea) was laminated onto the PDMS-coated temporary substrate. For the micropatterning of the PEDOT:PSS (Clevios PH-1000) on the PET

substrate, positive photoresist AZ-4620 was spin-coated on the PET substrate at 5000 rpm and baked at 110 °C 200 s. Using a mask aligner, the positive photoresist was exposed for 50 s and developed with AZ-300 MIF for 150 s. To enhance the adhesion and eliminate undeveloped photoresists, oxygen plasma treatment was performed with a reactive ion etch system with a 40 sccm O2 flow rate and RF power of 100-W for 60 s. Following the substrate treatment, PEDOT:PSS was spin-coated at 3000 rpm and baked at 100 °C for 5 min. The lift-off process was performed by immersing the sample in acetone and applying an ultrasonication process for removing the remaining photoresist except for the PEDOT:PSS patterning. To improve the electrochemical impedance and trace impedance of the PEDOT:PSS pattern, EG post-treatment was conducted at 100 °C for 20 min. Finally, the device was encapsulated using SU-8 2002, except for the neural sensing site (Sang et al., 2022). After the encapsulation process, the sample was hard-baked at 110 °C for 30 min for improved adhesion between the PEDOT:PSS and SU-8 layer.

2.2. Electrochemical impedance spectroscopy measurements setup

Electrochemical impedance spectroscopy (EIS) measurements of the PEDOT:PSS open-mesh electrode were conducted using a three-electrode system with a potentiostat (Gamry References 600+). A phosphate-buffered saline (PBS) solution was prepared by dissolving PBS powder in deionized (DI) water. In the three-electrode configuration, an Ag/AgCl electrode served as the reference electrode, a Pt wire as the counter electrode, and a PEDOT:PSS open-mesh electrode as the working electrode. The frequency sweep was performed from 1 Hz to 100 kHz, with measurements taken at 10 points per decade.

2.3. Simulation methods

The COMSOL simulation couples the Electromagnetic Waves module (frequency-domain) with the Bioheat Transfer module for the brain tissue, solving for the thermal response of brain tissue due to EM fields. The electrode placed inside the brain tissue experiences EM heating with heat transfer in the electrode and at the electrode/brain interface, which is simulated by the Electromagnetic Waves module (frequency-domain) with the Heat Transfer in the Solids module. The resonant frequency of interest is chosen to be 800 MHz. The heat flux from the electrode outflows into the electrode/brain tissue interface such that the exchanged conduction heat due to different EM heating between the electrode (source) and brain tissue (sink) reaches thermal equilibrium.

The temperature rise increases as the scale size (Fig. S1) or resonant frequency increases (Fig. S2). Scaling up MRI electrodes/implants (with increased scale size) increases their area to induce larger currents for increased temperature rise. On the other hand, increasing the frequency results in decreased skin depth (~1.3 mm for PEDOT:PSS at 800 MHz), which increases the resistance to further increase the temperature rise. Furthermore, increasing the frequency to 1 GHz results in a skin depth that becomes closer to the lateral dimensions of the electrode/implant, thereby drastically increasing the resistance and rapidly increasing the temperature rise.

2.4. In vitro MRI artifact imaging

In vitro MRI artifact imaging was conducted with a 9.4 T small animal MRI, BioSpec94/20USR (Bruker Biospin GmbH, Germany). For mesh electrode artifact comparison, T2 coronal imaging (spin echo) and susceptibility weighted coronal imaging (SWI, FLASH) were held. The parameters of T2 imaging are: TR: 2500 ms, TE: 33 ms, Flip Angle: 90° , FOV: 40 mm \times 40 mm, Slice thickness: 0.3 mm, Used coil: 72 mm receive coil. The parameters of SWI are: TR: 650 ms, TE: 11 ms, Flip Angle: 50° , FOV: 40 mm \times 40 mm, Slice thickness: 0.3 mm, Used coil: 72 mm receive coil. To make a hydrogen atom sufficient environment for *in vitro* imaging, an agarose-gel mold (thickness, 1 cm) was placed on

scaled-up Pt and PEDOT:PSS electrodes (electrode size, $1\times 1~{\rm cm}^2$, mesh electrodes fill factor, 30%). The Agarose-gel mold was obtained by using 1x TAE buffer (DYNE BIO, Korea) and Agarose-gel powder at 0.9% weight concentration.

2.5. RF electrode heating measurement

RF electrode heating was indirectly evaluated by resistance changes of electrodes. To make electrical contact, two wires were attached with silver paste to opposite edges of scaled-up Pt electrodes (electrode size, $1\times 1~{\rm cm}^2,~{\rm fill}$ factor, 30%). The scaled-up electrodes were heatinsulated by placing a 3 cm-thick PDMS block and Petri dishes on the electrode surface. The electrodes were stimulated by 10-W of RF energy. The RF energy was generated by using a 25 MHz sine wave by a function generator, a 10-W linear amplifier, and a commercial Tx coil. The resistance values were simultaneously recorded with the data acquisition system.

2.6. In-MRI temperature measurement

In-MRI electrode temperatures are measured inside a BioSpec 9.4 T small animal MRI. The MR-compatible temperature sensor was contacted on the center of scaled-up PEDOT:PSS electrodes (electrode size, $1\times 1~{\rm cm}^2,$ fill factor, 30%). The scaled-up open-mesh and closed-mesh electrodes are carefully loaded on the center of the MRI imaging station. Temperature measurements were held during high SNR T2 coronal imaging. The parameters of imaging are: TR: 4000 ms, TE: 22 ms, Average: 5, Flip Angle: 90° , FOV: $100~{\rm mm}\times45~{\rm mm},$ Slices: 50, Slice thickness: $0.3~{\rm mm},$ Resolution: $0.521~{\rm mm/pixel}\times0.234~{\rm mm/pixel},$ Used coil: $72~{\rm mm}$ receive coil.

2.7. Animal surgery

Two types of neural electrodes were used in the study. The first probe type was Pt with a diameter of 300 µm, and the second was the PEDOT: PSS neural probe with a width of 400 μm . This neural probe was implanted into the somatosensory region of the brain in Sprague-Dawley (SD) rats (Orient Bio, Gyeonggi-do, Republic of Korea; 8 weeks old; 200 g \pm 20 g). To precisely implant a flexible neural probe into the target site, a biodegradable probe coating was applied using polyethylene glycol (PEG). To achieve both the required mechanical stiffness for proper insertion and the desired impedance characteristics after PEG dissolution, a mixture of two different molecular weights of PEG was utilized. PEG with molecular weights of $(M_r = 4000)$ and $(M_r = 35,000)$, in a 1:1 mass ratio, was used for the device coating. This mixture was applied at temperatures above 100 °C. Rats were anesthetized with ketamine (100 mg/kg; Yuhan, Seoul, Republic of Korea), xylazine (10 mg/kg; Bayer Korea, Seoul, Republic of Korea) and isotropy 100 (Troikaa Pharmaceuticals Ltd, Gujarat, India). The animals were placed in a stereotaxic frame (WPI, Sarasota, FL, USA) when they reached surgical anesthesia levels. After the incision of the skin on the top of the skull, circular craniotomy with a diameter of 1-2 mm was performed on both sides based on bregma (Somatosensory region: based on bregma, anterior-posterior (AP) -2 mm; medial-lateral (ML) 5 mm; and depth (d) -1.5 - 1.8 mm). After the procedure, cefazolin (25 mg/kg; Chong Kun Dang, Seoul, Republic of Korea) was administered by injection for 5 days. The animals were housed in a facility accredited by the Association for Assessment and Accreditation of Laboratory Animal Care (AAALAC) in each center. All experiments were performed under the Institutional Animal Care and Use Committee (IACUC) approval (Protocol number: 2021-0311).

2.8. Verification of the transplanted location

To identify the implantation site of the neural probe, 1 week after probe transplantation, the brains were isolated by perfusing animals with saline followed by fixation with 4% paraformaldehyde (PFA, Merck, Darmstadt, Germany). Tissues were further fixed with 4% PFA for 24 h at 4 $^{\circ}$ C and then transferred to 30% sucrose in PBS for cryoprotection and stored for 1 week. Tissues were embedded in optimal cutting temperature compounds (Sakur Fineetek, Torrance, CA, USA), frozen at -80 $^{\circ}$ C, and cut in a 20 μ m thickness using a cryostat.

Tissues were dried for 2 h and then placed in acetone (Sigma-Aldrich, St. Louis, MO, USA) for 10 min. After rehydration with PBS for 10 min, it was stained with hematoxylin for $50 \, \text{s}$. After washing with DW for $5 \, \text{min}$, tissue was stained with eosin for $40 \, \text{s}$ and dehydrated with 70, 80, 90, and 100% grade ethanol (EtOH) solution. Clearing twice with xylene for $5 \, \text{min}$, mounted with permanently mounting medium (Fisher Scientific, Hampton, NH, USA).

The Cresyl violet/Eriochrome Cyanine staining, a nerve tissue-specific staining method, was also used to identify the implant location of the probe in the same way as the H&E staining method. The tissues were placed in acetone for 10 min to dehydrate and dried completely. Slides were stained with EC solution (MERCK, Kenilworth, NJ, USA) at 22 ± 2 °C for 30 min, and rinsed with running water. Samples were placed on 5% iron alum (Sigma-Aldrich) until the gray matter was observed and distinguished by treating borax-ferricyanide solutions (Sigma-Aldrich) for 5 min. Tissues rinsed with tap water and stained with cresyl violet (Sigma-Aldrich) for 1 min were differentiated using a 95% EtOH solution with a few drops of 10% acetic acid (Sigma-Aldrich) added. It was mounted after dehydration with a grade EtOH solution and cleaned with xylene in the same way as H&E staining. All the samples were observed under a light microscope (DM 2500; Leica, Wetzlar, Germany).

2.9. In vivo MRI artifact imaging

In vivo MRI artifact imaging was held with BioSpec 9.4 T small animal MRI. The Pt wire (diameter, 300 $\mu m)$ and PEDOT:PSS optimized neural probe (width, 400 $\mu m)$ were inserted into the left somatosensory cortex of 8 weeks 8-week-old rats. T2 imaging (spin echo) and SWI (FLASH) were held to compare quantities of image distortions. The parameters of T2 imaging are: TR: 2000 ms, TE: 20 ms, Flip Angle: 90°, FOV (Coronal): 35 mm \times 35 mm, FOV (Axial): 30 mm \times 30 mm, Slice thickness: 0.3 mm, Used coil: 20 mm planner surface coil & 86 mm coil. 10 ms, Flip Angle: 90°, FOV (Coronal): 35 mm \times 35 mm, FOV (Axial): 30 mm \times 30 mm, Slice thickness: 0.3 mm, Used coil: 20 mm planner surface coil & 86 mm coil.

2.10. Confirmation of the immune response at the implanted site

TUNEL staining was used to detect cell death of the brain by implanted probes. TUNEL assay was performed according to the manual (TUNEL-FITC, ab66108, Abcam, Cambridge, UK). Sections were washed 3 times for 10 min, followed by 2 times treatments for 30 min with wash buffer. Sections were then incubated in a humidified atmosphere with a mixture of staining solution (Reaction Buffer, TdT Enzyme, FITC-dUTP, and ddH2O) for 60 min at 37 °C in the dark. The sections were then rinsed three times with rinse buffer and the Propidium iodide/RNase A solution was reacted for 30 min at room temperature. To confirm the total number of cells, tissues were mounted with the mounting medium with 4,6-Diamino-2-phenylindole (DAPI). Tissues were observed under confocal laser scanning microscopy (LSM700, Carl Zeiss, Oberkochen, Germany) and analyzed using ImageJ (RRID: SCR_003070, NIH, Maryland, USA).

2.11. Electrophysiological recording and electrical stimulation system setup

To measure electrophysiological signals, the fully MRI-compatible PEDOT:PSS neural probe and a reference wire were inserted into the somatosensory cortex region of a rat's brain. Electrophysiological signals ranging from 0.1 Hz to 6000 Hz were recorded using the Intan RHS recording and stimulation system. A 60 Hz notch filter was applied to minimize AC noise from the environment. Simultaneously, biphasic electrical stimulation of the hind-paw was performed using the same Intan RHS recording and stimulation system. For this stimulation, two-needle electrodes were employed, configured to produce opposite phases with the same stimulation amplitude: 1 mA cathodic-anodic and 1 mA anodic-cathodic. Stimulations were delivered every second with a duration of 1 ms.

2.12. Statistical analysis

The electrochemical impedance, phase, and simulation graphs were plotted using Origin Lab. Software. Electrochemical impedance and phase plots of the square, closed-mesh, and open-mesh designs were plotted as average values, n=10 electrode samples. Immune response data are presented as mean \pm standard error of the mean (SEM). Differences between groups were evaluated by one-way analysis of variance (ANOVA) with Tukey's multiple comparisons tests were performed using GraphPad Prism 10.2 for Windows (GraphPad Software, USA). The measured electrophysiological recording data were analyzed using MATLAB software. A Butterworth low-pass filter with n=3 and f=250

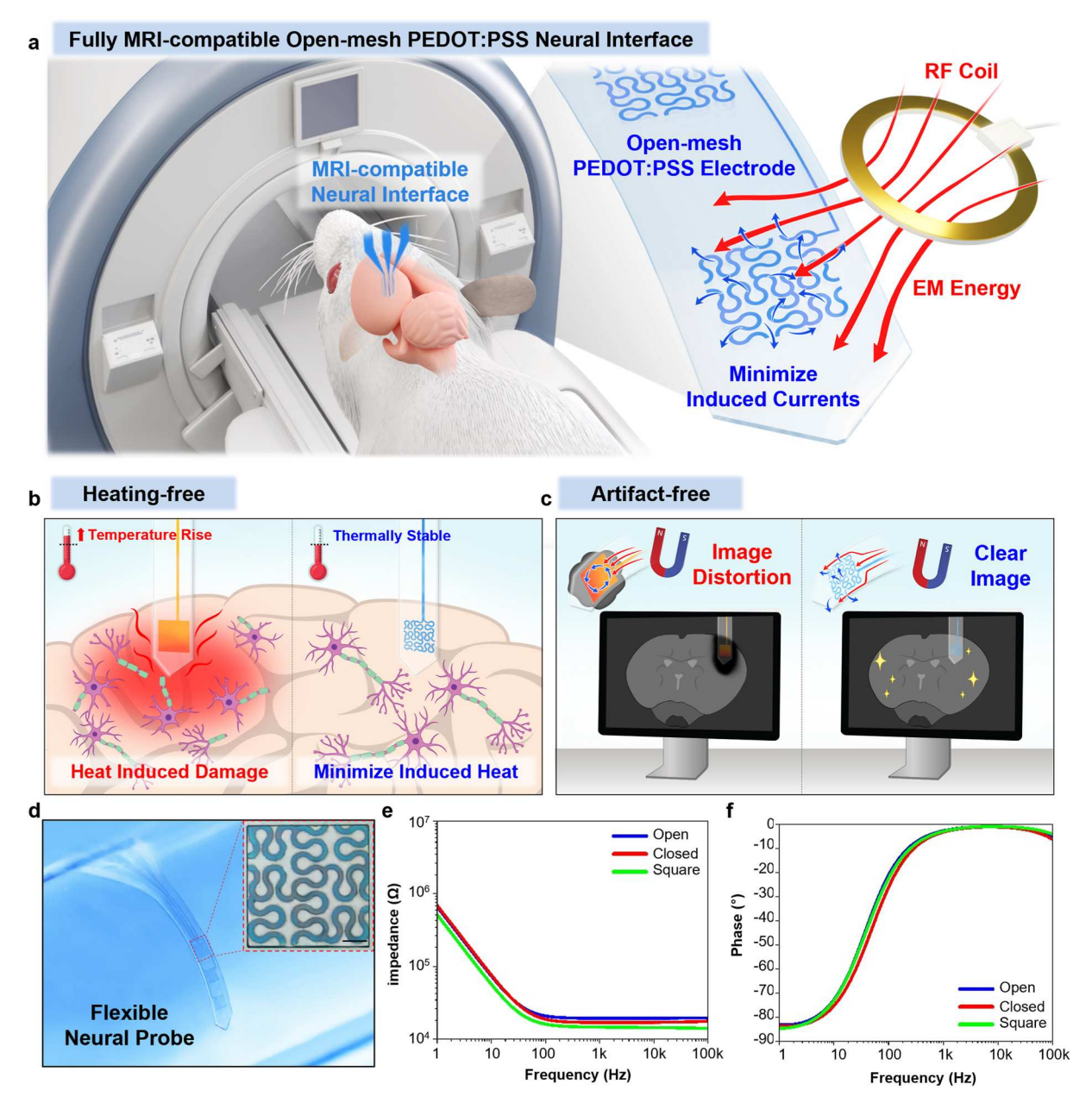


Fig. 1. Fully MRI-compatible open-mesh PEDOT:PSS neural interface. (a) Schematic illustration of fully MRI-compatible open-mesh PEDOT:PSS neural interface. Induced currents are minimized in the MRI environment because of closed loop avoiding open-mesh structure. (b) Schematic illustration of heating-free characteristics. (c) Schematic illustration of artifact-free characteristics. (d) An image of a fully MRI-compatible open-mesh neural probe on a transparent grassy rod (diameter, 3 mm). A microscopic image of an open-mesh electrode is inserted inside a dashed red box. Scale bar, 50 μm. (e) Electrochemical impedance plot of PEDOT:PSS open-mesh, closed-mesh, and square electrodes by EIS measurements. Averaged 10 channel impedances for each structure (square, 14.64 kΩ; closed-mesh, 16.99 kΩ; open-mesh, 19,34 kΩ at 1 kHz). (f) EIS phase plot of PEDOT:PSS open-mesh, closed-mesh, and square electrodes. Averaged 10 channel phases for each structure.

Hz was employed for appropriate LFP analysis. Additionally, the power spectral density plotting was conducted through MATLAB and the Intan RHX software.

3. Results and discussion

3.1. Fully MRI-compatible open-mesh PEDOT:PSS neural interface

Fig. 1a presents a schematic illustration of the fully MRI-compatible monolayer open-mesh pristine PEDOT:PSS neural interface. This PEDOT:PSS open-mesh neural interface is fabricated based on the conductive polymer material PEDOT:PSS. PEDOT:PSS inherently possesses low electrical conductivity; however, through post-treatment processes, its electrochemical impedance is improved, enabling it suitable for use in neural implants (Bianchi et al., 2022). Furthermore, because of its low electrical conductivity and similar magnetic susceptibility to soft tissues, PEDOT:PSS is recognized as a material with high MRI compatibility (Cho et al., 2024b). In the development of MRI-compatible electrodes, it is also crucial to enhance the MRI compatibility of neural interface through structural modifications (Tian et al., 2019). Therefore, by utilizing the high MRI compatibility of PEDOT:PSS and its compatibility with photolithography-based micropatterning, a fractal open-mesh electrode structure that avoids closed loops was combined with the neural implant. This design minimizes induced currents and side effects from the MRI environment, resulting in a fully MRI-compatible neural probe in terms of both material and structure optimization.

The fully MRI-compatible open-mesh PEDOT:PSS neural interface offers two remarkable advantages in the MRI environment: 1) minimized induced heating and 2) artifact-free imaging. Fig. 1b represents the thermal stability of the fully MRI-compatible neural probe in MRI. In the MRI environment, which uses strong EM energy, RF-induced heating is a critical concern for neural implants (Winter et al., 2021). This heating effect is substantially influenced by electrical conductivity of the material used. The SAR, a metric intimately associated with the heat produced in the tissue surrounding the implant, is directly influenced by the material's conductivity, as delineated in Eq. (1) (Seo and Wang, 2021). Consequently, the elevated conductivity of the neural interface resulted in a substantial rise in heat generation within the MRI environment.

Metal electrodes, commonly employed in neural implants, are highly vulnerable to heating in MRI environment because of their high electrical conductivity (Zhang et al., 2021). In contrast, PEDOT:PSS exhibits relatively lower electrical conductivity, resulting in lower heat generation in the MRI environment (Cho et al., 2024b). Despite the relatively low electrical conductivity of PEDOT:PSS compared to other conventional metals, concerns about the potential for neural implant applications can be compensated by the material properties and suitable post-treatment of PEDOT:PSS. PEDOT:PSS exhibits multiscale phase separation between PEDOT-rich and PSS-rich phases, facilitating the formation of an electrical double layer at the interface. This feature results in a large effective capacitance, enabling sufficiently low electrochemical impedance (Bianchi et al., 2020; Volkov et al., 2017). Moreover, EG post-treatment and relatively large surface area of PEDOT:PSS, in comparison to metal electrodes, further reduce the electrochemical impedance suitable for neural implant applications (Cho et al., 2022a).

Beyond excellent material characteristics of PEDOT:PSS that minimize heating in MRI environments, structural enhancements in the electrode design further contribute to its thermal stability. Induced currents from the implants in the MRI environment can lead to tissue damage surrounding the electrode, either through self-heating of the electrode or through leakage currents (Dempsey and Condon, 2001; Winter et al., 2021). Therefore, minimizing these induced currents is critical for ensuring thermal stability in MRI applications. According to Faraday's law (Eq. (2)), electrode structure that reduces the closed

contour loop area (CCLA) in an MRI environment can reduce the induced currents. The open-mesh electrode structure effectively reduces CCLA, therefore minimizing of induced current generation caused by the strong EM energy (Tian et al., 2019). In essence, this work achieves optimized thermal stability by adopting materials and structures that are thermally stable in the MRI environment.

Fig. 1c illustrates that our neural probe enables artifact-free MRI. The occurrence of MRI artifacts due to electrode implants is primarily attributed to magnetic field imperfections (Zhang et al., 2021). Magnetic susceptibility is a parameter that denotes the direction and magnitude of magnetization occurring because of a surrounding magnetic field (Deistung et al., 2017). Therefore, the mismatch in magnetic susceptibility between the tissue and electrode leads to unintended magnetic field distortions when exposed to the external magnetic fields of the MRI environment, contaminating the MRI images. For instance, Pt, one of the biocompatible metals commonly used for neural recording electrodes, is a paramagnetic material with positive susceptibility (279 ppm) (Zhang et al., 2021). Soft tissues, such as the brain tissues, are known to possess a weak negative magnetic susceptibility (-7 to -11 ppm). Therefore, implanting a neural probe made of Pt can cause substantial imaging artifacts because of susceptibility mismatch. In contrast, PEDOT:PSS is a diamagnetic material with weak negative susceptibility (-0.0037 ppm)and has a minor difference in the magnetization rate with surrounding soft tissues, making it less likely to distort images because of material properties and thus suitable for the development of MRI-compatible electrodes (Cho et al., 2024b). The phenomenon of magnetic field inhomogeneity in the MRI environment should also be minimized through appropriate material selection and structural optimization of the electrode as well. Induced currents generated within the electrode in an MRI environment, which are highly related to CCLA as detailed in Eq. (2), induce secondary magnetic fields. These induced magnetic fields can lead to additional magnetic field inhomogeneity, adversely affecting the image quality (Tian et al., 2019). Therefore, the specialized electrode structure of the PEDOT:PSS open-mesh neural probe, which minimizes induced currents, can reduce the secondary induced magnetic fields and help achieve completely artifact-free imaging.

The PEDOT:PSS open-mesh neural probe comprises three open-mesh electrodes micropatterned on the flexible PET substrate (electrode size: $250 \times 250 \ \mu m^2$, fill factor, 30%, Fig. 1d). Each mesh electrodes were fabricated by patterning with 10 µm linewidth using PEDOT:PSS solution through ultrasonication lift-off process (Fig. S3). Subsequently, the micropatterned PEDOT:PSS electrodes are treated with EG solution to ensure adequate electrochemical impedances for neural interface applications without compromising MRI compatibility (Cho et al., 2024b). To precisely evaluate the electrophysiological measurement performance of mesh-patterned electrodes, electrochemical impedance and phase for various patterns were compared using EIS measurements (Fig. 1e and f). The EG post-treated PEDOT:PSS electrodes patterned with closed-mesh and open-mesh structures were compared against the most conventionally used electrode pattern in neural recording, the square electrode, as a reference. Despite the mesh structure electrodes having an area approximately 30% of that of the square electrode, they displayed a similar level of impedance performance (square, 14.64 kΩ; closed-mesh, 16.99 k Ω ; open-mesh, 19.34 k Ω at 1 kHz, 10 channel impedances are averaged for each structure). This indicates that the mesh structure electrodes not only possess high MRI compatibility but also demonstrate sufficient performance as electrophysiological measurement neural implants.

3.2. Material selection

With a brain tissue phantom placed inside an air medium with three EM wave-generating coils in each axis (Fig. 2a), EM heating is simulated using COMSOL Multiphysics (Note. S1) (Cho et al., 2024b; Choi and Konrad, 1991; Lottner et al., 2022). The exposure of the system to the coil generates the SAR and temperature rise on Pt electrodes and

Perfectly Matched Layer Z-axis Coil RF Heating RF Heating

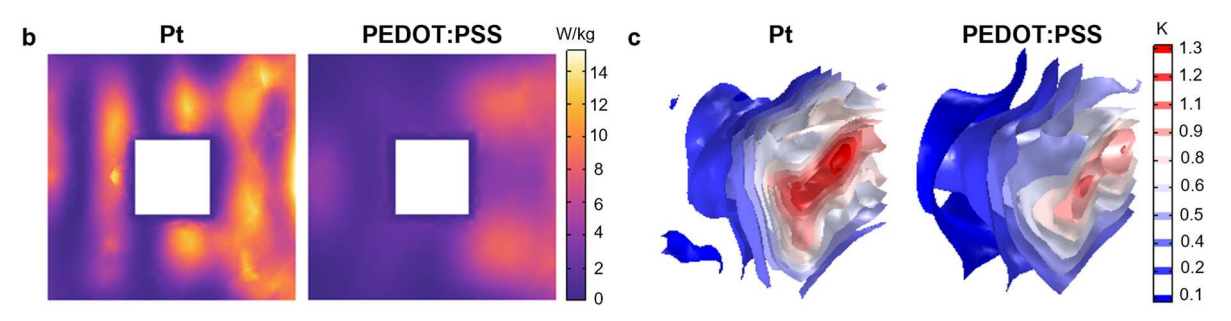


Fig. 2. Simulation setups and simulations for material selection. (a) Simulation setup. Three EM wave-generating coils are placed inside a perfectly matched layer, each port delivers EM waves along the x, y, and z axes directions. The electrode to proceed simulation is placed at the center of the brain tissue phantom. (b) SAR simulation comparing the Pt and PEDOT:PSS electrodes. (c) Temperature rise simulation Pt and PEDOT:PSS electrode.

PEDOT:PSS electrodes placed inside the brain tissue (Fig. 2b and c and Note. S2 and S3) because of EM heating. The PEDOT:PSS electrode shows lower SAR across the brain tissue than Pt electrodes. The brain tissue with the PEDOT:PSS electrode shows a peak SAR of 19.4 W/kg, which is around 53% lower than 41.1 W/kg from the Pt electrode. The SAR exposure is also consistent in the plane parallel to the x-axis coil (Fig. S4). Furthermore, a similar trend in temperature rise is observed in the comparison between the two electrodes. The PEDOT:PSS electrode creates a maximum temperature rise of around 0.9 K in the brain phantom, which is around 36% lower than 1.4 K in the brain phantom carrying the Pt electrode. Along with these parameters, PEDOT:PSS electrodes provide superior MRI compatibility compared to Pt electrodes in terms of the magnetic field across the brain tissue (Fig. S5), resulting in lower total heat flux magnitude (Fig. S6) and induced current magnitude (Fig. S7).

3.3. Electrode pattern optimization

Although PEDOT:PSS electrodes could improve the MRI compatibility of the probe compared to Pt electrodes, the patterns of the probes can still be designed and optimized to further improve the performance. By leveraging the photolithography process, closed design and different open designs have been fabricated and compared to block designs discussed previously. CCLA plays a key role in optimizing the induced current (Galili et al., 2006; Pearce Williams, 1963; Sophian et al., 2001). CCLA is defined as the apparent area of any smooth, simple closed surface bounded by a continuous contour line lying inside the design domain (Zhao et al., 2011). For the same apparent area (0.09 mm²), perimeter (5 mm), and fill factor (30%), closed designs have a CCLA of πr^2 or equivalent to the area of a circular block structure of radius r,

whereas the open designs have an approximate CCLA of $2\pi rd$ ($d\ll r$ is the width) (Fig. 3a). Therefore, the open design reduces CCLA to $2d/r\ll 1$ compared to the closed design. Furthermore, there is still a scope to improve the open design mesh structure by optimizing the connections or intersections of the traces in the mesh structure. COMSOL Multiphysics simulation is employed to optimize the mesh design structure and further the mesh connections to minimize the temperature rise and induced voltage/current, subsequentially image artifacts. According to Faraday's law of induction, the total induced voltage φ due to an alternating EM field is given by (Fleisch, 2008; Shi et al., 2015):

$$\varphi = \oint_{\partial \Pi} \overrightarrow{E} \bullet \overrightarrow{dl} = -\iint_{\Pi} \frac{\partial \overrightarrow{B}}{\partial t} \bullet \overrightarrow{dA} = -\sum_{i=1}^{N} \iint_{\Pi_{i}} \frac{\partial \overrightarrow{B}}{\partial t} \bullet \overrightarrow{dA}$$
 (Eq. 3)

where \overrightarrow{E} and \overrightarrow{B} are the electric and magnetic field through the CCLA vector $\overrightarrow{\Pi}$ composed by the series of elemental CCLA $\Pi = \sum_{i=1}^{N} \Pi_i$, where the element $i \in [1, N]$ denotes each closed contour loop enclosed by a closed loop line l_i ensemble spanning the CCLA. Intersection marks are defined at any intersection or connecting point in the optimized mesh structure except the center without loss of any generality. These intersection marks define each elemental CCLA region in the mesh structure. For the same total length and CCLA, open-mesh structures can be varied in three different structures: unoptimized open-mesh I, II, and optimized open-mesh, which are comprised of 9, 5, and 4 intersections or connections, respectively (Fig. 3b). For example, unoptimized open-mesh I has 9 elemental CCLA (Fig. S8) separated by intersection points except the center. The elemental CCLA Π_i is surrounded by elemental contour line $\partial \Pi_i$ (Fig. S9). Even though the area, perimeter, and fill factor of all three open-mesh structures are equal, optimized open-mesh shows the best performance, which can be attributed to the equal area and

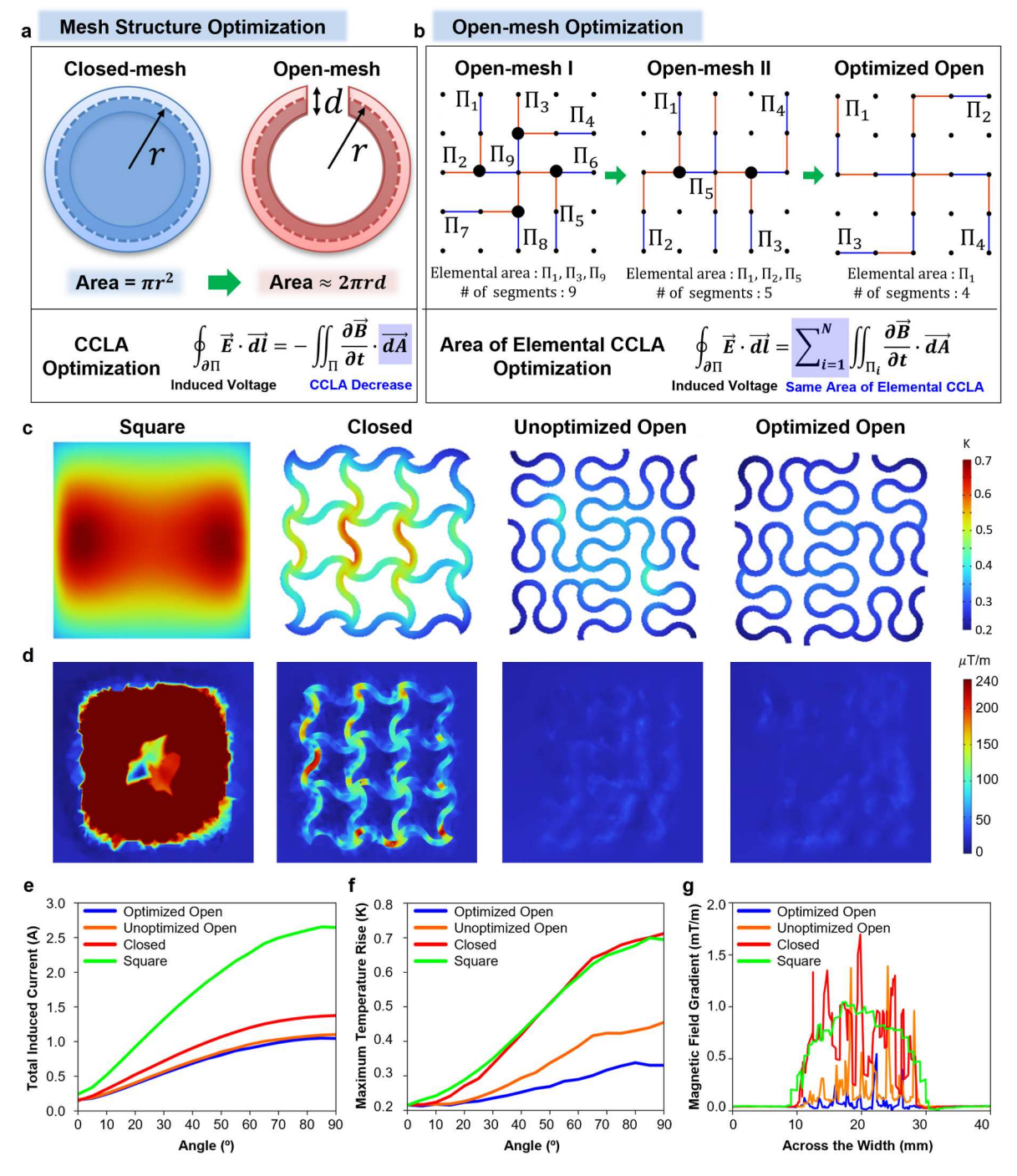


Fig. 3. Simulations for pattern optimization. (a) Mesh structure optimization theory. The open-mesh structure effectively reduces the closed contour loop area (CCLA). A decrease in CCLA yields lower induced voltage in an MRI environment. (b) Open-mesh optimization theory. Even though each open-mesh pattern has identical CCLA, optimized open-mesh evokes the lowest induced voltage in the MRI environment because of the same area of elemental CCLA matching arithmetic mean-geometric mean inequality. (c) Temperature rise simulations with identical scale. (d) Magnetic field gradient simulations with identical scale. (e) Total induced current simulations for various electrode patterns. (g) Magnetic field gradient simulations for various electrode patterns.

minimum number of elemental CCLA (i.e., $\Pi_1 = \Pi_2 = \Pi_3 = \Pi_4$). Following an arithmetic mean-geometric mean inequality (Djukić et al., 2006), the induced voltage is optimized for optimized open-mesh as:

$$\iint_{\Pi_1} \frac{\partial \overrightarrow{B}}{\partial t} \bullet \overrightarrow{dA} = \iint_{\Pi_2} \frac{\partial \overrightarrow{B}}{\partial t} \bullet \overrightarrow{dA} = \iint_{\Pi_2} \frac{\partial \overrightarrow{B}}{\partial t} \bullet \overrightarrow{dA} = \iint_{\Pi_4} \frac{\partial \overrightarrow{B}}{\partial t} \bullet \overrightarrow{dA}$$
 (Eq. 4)

The theoretical analysis is validated by the COMSOL Multiphysics simulation results (Carrizales and Lake, 2009; Kennedy et al., 2011;

Salvi et al., 2011). From a design perspective, the MRI compatibility of optimized open-mesh is superior to unoptimized open-mesh II and open-mesh I and has a 46% lower electric field magnitude compared to closed-mesh (Fig. S10). Compared to the optimized open mesh, the unoptimized open mesh I and II have 14.3% and 11.5% higher maximum electric field magnitude, respectively. The electric field variation is reflected in the temperature rise profile across the square, closed-mesh, and open-mesh structures (Fig. 3c). Closed-mesh and square structures with the same but large CCLA generate the highest

peak temperature rise of approximately 0.7 K, whereas the optimized open-mesh with 70% smaller CCLA has a maximum peak temperature rise of 0.3 K, only 0.1 K higher than that of 0.2 K for the control tissue (without any electrode). The unoptimized open mesh I has a maximum peak temperature of 0.46 K, 53% higher than the optimized open mesh. Different from the temperature rise profile that is difficult to evaluate in the experiment, image artifacts in MRI are much more straightforward

from an experimental standpoint. However, MRI images are created through various phase and frequency encoding, making them almost impossible to simulate exactly. A more practical approach is to evaluate the image artifact using the magnetic field gradient (Hidalgo-Tobon, 2010; Turner, 1993). From a fundamental standpoint, the three-directional gradient coils in MRI are primarily used to map the spatial map of the specimen. Therefore, induced changes in the magnetic

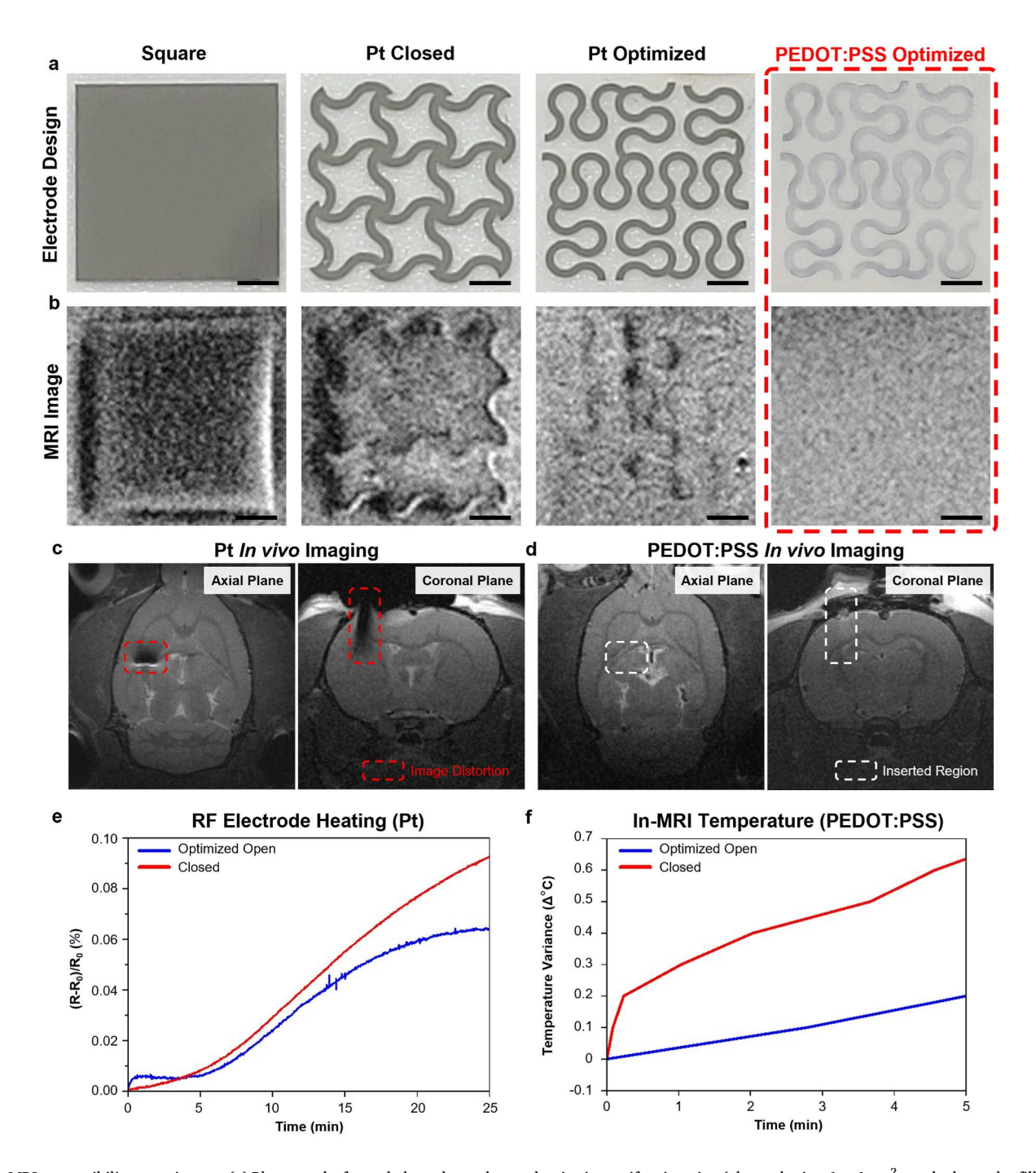


Fig. 4. MRI compatibility experiments. (a) Photographs for scaled-up electrodes used as *in vitro* artifact imaging (electrode size, $1 \times 1 \text{ cm}^2$, mesh electrodes fill factor, 30%). From the left, Pt square, Pt closed, Pt optimized open, PEDOT:PSS optimized open. Scale bar, 2 mm. (b) *In vitro* T2 Flash MRI image artifacts comparison. From the left, Pt square, Pt closed, Pt optimized open, PEDOT:PSS optimized open. Scale bar, 2 mm (c) *In vivo* T2 Flash MRI image artifact of Pt wire inserted in a rat at its somatosensory cortex (diameter, 300 μ m). The dashed red box marks the image distortion area. (d) *In vivo* T2 Flash MRI image without image artifact for fully MRI-compatible open-mesh neural probe inserted in a rat at the somatosensory cortex (probe width, 400 μ m). Dashed white box shows the probe inserted region. (e) RF electrode heating test for scaled-up open-mesh and closed-mesh Pt electrodes (electrode size, $1 \times 1 \text{ cm}^2$, fill factor, 30%). Higher resistance change implies higher temperature increment due to the positive thermal-resistance coefficient of Pt. (f) In-MRI temperature measurement for scaled-up open-mesh and closed-mesh PEDOT:PSS electrodes (electrode size, $1 \times 1 \text{ cm}^2$, fill factor, 30%).

field would be reflected in the disturbance in the phase and frequency mapping, thereby distorting the image. The magnetic field gradient map also reflects a similar trend where the square and closed-mesh structures have a 270 μ T/m or 718% higher than 33 μ T/m from the optimized open-mesh (Fig. 3d). The unoptimized open mesh I also has a maximum magnetic field gradient magnitude of 62 μ T/m, which is 88% higher than the optimized open mesh. In this simulation, we have rotated the probe at different angles of exposure where the projected area in the x-direction increases (Fig. S11). With just the x-axis EM coil turned on, the total induced current increases with the increasing angle as the projected area between the coil and the electrode increases, which is reflected in the increase of the magnetic flux $(\overrightarrow{B}.\overrightarrow{dA})$ following an approximate sine curve) (Fig. 3e). The induced current of 2.6 A for the square structure is the highest: 86% higher than 1.4 A from the closed-mesh structure and 150% higher than 1.04 A from the optimized open-mesh structure. The induced current of unoptimized open-mesh is 5.7% higher compared to optimized open-mesh. Similarly, the maximum temperature rise increases with the increasing projected angle (Fig. 3f). At the projected angle of 45°, the closed and square structures exhibit a temperature rise of 0.5 K, which is almost twice of 0.27 K from the optimized open mesh. Moreover, the maximum temperature at this angle for open mesh I is 0.31 K, which is 14.8% higher than the optimized mesh structure. The magnetic field gradient across the electrode length is further calculated to provide insights into the image distortion (Fig. 3g). The square and closed structures have a much higher field gradient compared to open-mesh structures. Furthermore, the square structure has a spatially broader field gradient (and a broader image distortion) than a closed-mesh structure (Turner, 1993). Although more comprehensive studies are still needed to improve the image distortion simulation further, the concepts from this study can provide a basic framework to replicate the MRI imaging technique for understanding and optimizing MRI-compatible neural electrodes and implants.

3.4. MRI compatibility test

Fig. 4 shows data related to imaging and temperature measurement to experimentally validate the simulation results of MRI compatibility arising from differences in the material and the electrode patterns. Fig. 4a and b illustrate the differences in artifacts due to material and pattern changes of Pt electrodes and PEDOT:PSS electrodes in MRI T2 imaging. The experiment utilized enlarged electrode patterns of 1×1 cm² size to observe clear changes according to the differences in the material and the pattern. Based on the nature of MRI, which captures images using the alignment and recovery signals of hydrogen atoms, it is essential to provide an adequate hydrogen environment around the electrode. Therefore, for in vitro MRI imaging, an agarose gel mold was placed over the electrode for imaging. In the case of square Pt electrodes, typically used as neural measurement electrodes, strong image distortions occur not only around the electrode but also within the electrode area. Similarly, closed-mesh Pt electrodes also exhibited strong image distortions inside the closed loop region. In contrast, Pt electrodes patterned with the optimized open-mesh structure through simulation showed significantly reduced imaging artifacts compared to the previous two cases. The simulation of structural changes confirmed that reduction of induced currents according to the electrode structure influences the imaging results. This experiment experimentally proves that, similar to the simulation results, imaging artifacts can be optimized according to the electrode structure in the MRI environment. Subsequently, MRI performance of the PEDOT:PSS optimized electrode, based on the structurally optimized open-mesh electrode structure, was confirmed. The experimental results demonstrated that the PEDOT:PSS optimized open-mesh electrode presented a completely clean image without any distortion (Figs. S12 and S13). This result confirms that the complete optimization of imaging artifacts is achieved through

combining the structural modifications with the material's excellent MRI compatibility.

Fig. 4c and d compare the imaging artifacts of Pt electrodes and PEDOT:PSS-based optimized electrodes through *in vivo* MRI. The Pt electrodes for control images and our PEDOT:PSS-based optimized electrodes are inserted up to a depth of 2 mm into the somatosensory cortex area of a rat, followed by MRI. For control images intended for comparison, a Pt wire with a diameter of 300 μm , less than the width of our optimized device of 400 μm , was inserted. The results showed black image contamination in the control images (Figs. S14 and S15), with these artifacts occurring over a much wider area than the actual region of electrode insertion. In contrast, our PEDOT:PSS-based optimized neural probe allowed for completely clear, artifact-free MRI when observing the same insertion area. This demonstrated the achievement of image artifact optimization in actual *in vivo* MRI.

To evaluate the performance of electrodes in suppressing heat generation according to their mesh structure, further experiments were conducted. Similar to the methodology employed in the *in vitro* imaging artifact experiments, these experiments utilized enlarged electrode patterns measuring 1×1 cm² to clearly observe the changes in heat generation associated with various patterns. Fig. 4e presents the experimental results showing the differences in heat generation according to the mesh structure of Pt electrodes under an RF environment to mimic MRI conditions. Pt, known for its positive temperature coefficient of resistance, exhibits an increase in resistance in response to temperature elevations (Mailly et al., 2001). Therefore, the substantial change in resistance observed in the electrodes can be interpreted as a reflection of considerable fluctuations in electrode temperature. The experiment was performed by applying same RF energy to optimized open-mesh and closed-mesh electrodes. When 10-W RF energy was applied to two patterns for 25 min, the closed-mesh electrode exhibited a resistance change of approximately 0.0926% compared to the baseline, while the open-mesh electrode showed a resistance change of approximately 0.0644% compared to the baseline. The findings revealed that the open-mesh electrode demonstrated a lower rate of resistance change compared to the closed-mesh electrode, indicating the superior heat suppression characteristics of the open-mesh electrode.

Additionally, an in-MRI temperature experiment was conducted to assess the differences in temperature changes according to the mesh structure in an actual MRI environment. The experiment involved measuring temperature changes of an PEDOT:PSS open-mesh electrode and closed-mesh electrode over the duration of an MRI scan. Consistent with the results of prior simulations and RF electrode heating tests, a higher temperature change was observed in the closed-mesh electrode. When subjected to strong EM energy for 5 min inside the MRI, the closed-mesh electrode exhibited a temperature change of approximately 0.6 °C, whereas the open-mesh electrode showed a temperature change of about 0.2 °C. This result demonstrates thermal stability of the PEDOT: PSS-based open-mesh electrode in a real MRI setting.

We experimentally demonstrated that our PEDOT:PSS open-mesh electrode design, which was created through modifications in material and structure, exhibits high compatibility within an MRI environment. The integration of PEDOT:PSS with an open-mesh structure, which avoids closed loops, effectively minimizes artifacts during MRI scans, even in the presence of strong EM waves. Furthermore, our experimental results indicate that PEDOT:PSS open-mesh electrode possesses significant heat suppression characteristics in an MRI environment. This demonstrates that our innovative design, which is fully compatible with MRI, ensures the stable acquisition of clear images with minimal temperature changes during MRI scans.

3.5. In vivo experiments

Fig. 5 includes the results of electrophysiological recording *in vivo* experiments using a fully MRI-compatible PEDOT:PSS-based neural probe. The somatosensory cortex region is an area where neuronal

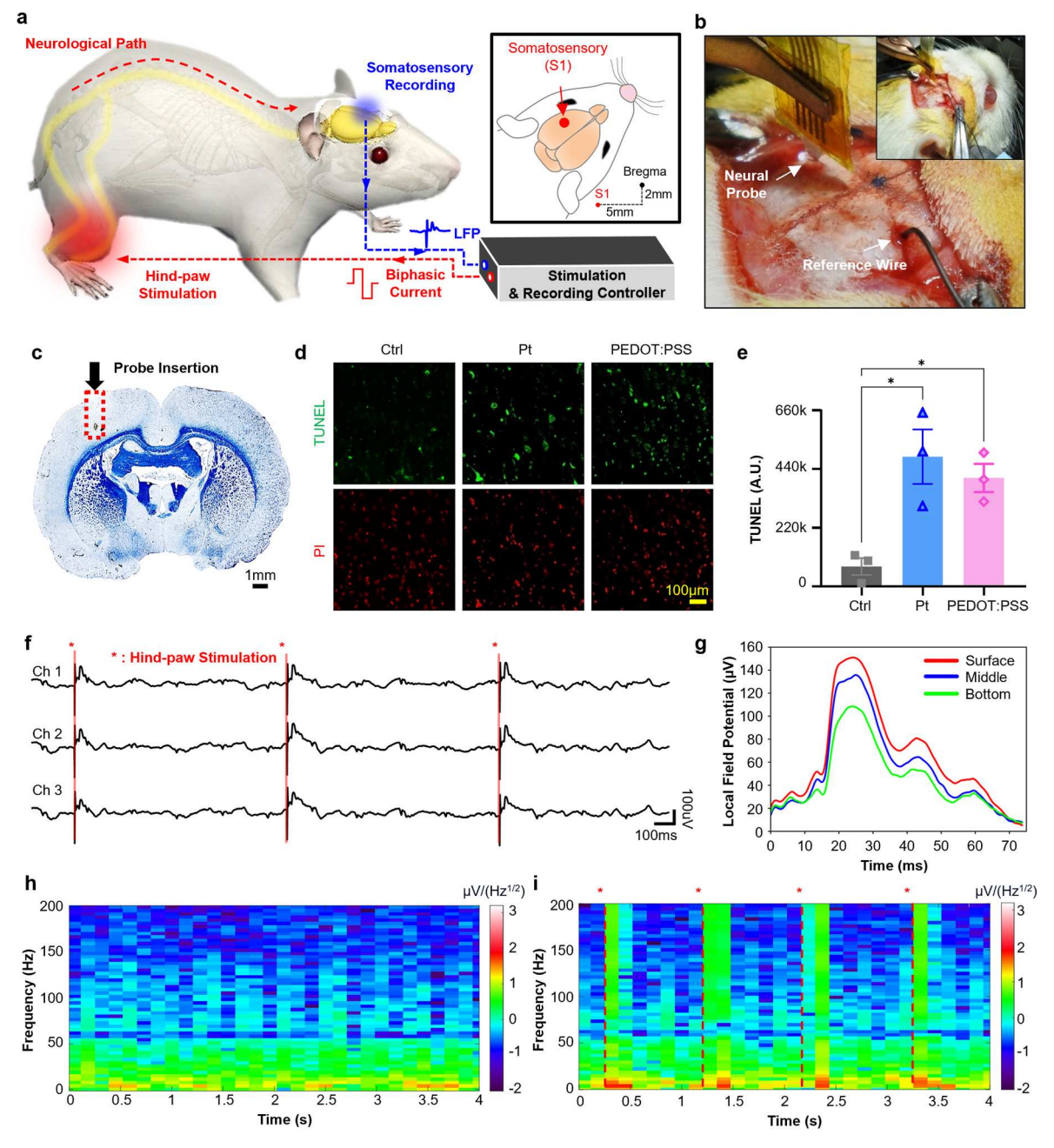


Fig. 5. In vivo experiments for electrophysiological recording. (a) Schematic illustration of in vivo experiment. A fully MRI-compatible open-mesh neural implant is inserted into the somatosensory cortex (S1). Simultaneous LFPs recording is conducted during hind-paw electrical stimulation with 1 Hz biphasic current. The inserted schematic illustration shows the location for device insertion on an 8-week rat. (b) Photographs for in vivo recording experiment. A fully MRI-compatible open-mesh neural probe is inserted into the left S1 region to record the electrophysiological signal evoked by right hind-paw stimulation, and a reference wire is inserted into the right S1 region. (c) Neural probe implanted site (red box) in Cresyl violet. (d) Confocal images of the probe implant areas in each group (Ctrl, Pt, and PEDOT:PSS) stained with TUNEL (green) and propidium iodide (red). (e) Mean intensity of the TUNEL in each group. All data are expressed as mean \pm S.E.M. *P < 0.05. (f) 3-channel LFP recording during 1 Hz hind-paw electrical stimulation. Hind-paw stimulated points are marked as dashed red lines. (g) Stacked LFP signals evoked right after single biphasic electrical stimulation. (h) Power spectral density for spontaneous LFP signal under anesthesia. (j) Power spectral density plot for LFP with simultaneous 1 Hz hind-paw electrical stimulations. Dashed red lines imply electrical stimulations.

signals are activated in response to the stimulation of the opposite-site whiskers or the hind-paw (Lee et al., 2022; Moxon et al., 2008). To evaluate the neural recording performance of the fully MRI-compatible neural probe, the device is inserted at a depth of 2 mm into the left somatosensory cortex region of an anesthetized SD rat and records the changes in LFPs in response to electrical stimulation of the right hind-paw is recorded (Fig. 5a). For precise insertion of the flexible neural probe, PEG was coated on the neural probe to provide sufficient stiffness. PEG is a biodegradable polymer that completely dissolves after

the insertion process, enabling precise placement and recording (Guan et al., 2019; Seo et al., 2019). Furthermore, by examining the 1 kHz electrochemical impedance in relation to the dissolution of PEG, it was verified that the electrochemical functionality of the device was effectively recovered after biodegradation of the PEG coating (Fig. S16). Fig. 5b shows a photograph of the setup for the *in vivo* experiment. The device was inserted into the left somatosensory cortex region of the rat using a biodegradable PEG coating, and a reference electrode was inserted into the opposite somatosensory cortex region. Neuronal signal

activation in the left somatosensory cortex region was measured in response to the right hind-paw electrical stimulation process.

To ensure that the neural probe was correctly implanted in the somatosensory region of the cerebral cortex (Cx) and confirm the further damage in tissue during the implant, tissues were sectioned and stained (Fig. S17). Through cresyl violet/EC staining and H&E staining, the neural probe was implanted in the Cx region to the extent that it did not reach the corpus callosum (-1.5 to 1.8 mm). It was confirmed that no immune response and additional tissue damage occurred at the implantation site (Fig. 5c). Additionally, nerve probe implanted sites were examined by TUNEL assay compared to the right cerebral hemisphere (Ctrl) that did not implant probes to analyze apoptosis. The results confirmed that the PEDOT:PSS-based neural probe had no problems with cytotoxicity and immune response (Fig. 5d and e and S18).

Fig. 5f represents the LFP from the somatosensory cortex region in response to hind-paw electrical stimulation. Each channel shows a depth difference of 0.5 mm, with the bottom electrode measuring signals from a depth of 1.8 mm. When a 1 mA electrical stimulation was applied to the hind-paw once per second, changes in the LFP due to the electrical stimulation were observed. Fig. 5g is an overlapped graph of the LFP signals from one electrical stimulation with various electrodes. The depth of the electrode correlated with a decrease in the amount of LFP change in the same stimulation. Additionally, to confirm the neuronal activation of the brain, a comparison between spontaneous activity and electrically stimulated LFP activity was analyzed using a spectrogram. Fig. 5h and i presents the results of the spectrogram of the spontaneous and electrically stimulated LFP activity. In Fig. 5h, in the absence of stimulation, the LFP signal maintains a consistent signal value over time. However, in Fig. 5i, which includes a 1-s interval of electrical stimulation, there is a clear power change in the low-frequency band following the electrical stimulation point.

4. Conclusions

This study presents the fabrication of neural implants that exhibit exceptionally high compatibility within MRI environments. The combination of PEDOT:PSS and an open-mesh structure leverages the material characteristic of low conductivity and magnetic susceptibility similar to those of soft tissue, along with structural advantages. These characteristics help in minimizing the generation of induced currents in the MRI environment. The reduction of induced current not only allows for the acquisition of clear and undistorted MRI images but also minimizes the risk to patients from heating during MRI scans. Furthermore, the fully MRI-compatible neural probe developed in this study ensures sufficient electrochemical impedance, through EG post-treatment, further facilitating high-quality *in vivo* electrophysiological recording.

Initial simulations confirmed the material difference between the PEDOT:PSS and Pt electrodes and the open-mesh design, by minimizing the CCLA, successfully enhanced MRI compatibility compared to other electrode patterns. Additionally, simulations demonstrated that an open-mesh design with the same area of elemental CCLA is most advantageous in MRI environments, thus optimizing electrode patterns. Subsequent in vitro MRI experiments showed that transitioning from conventional square electrodes to an open-mesh electrode progressively reduced MRI artifacts. Additionally, it was experimentally confirmed that PEDOT:PSS electrodes with an optimized open-mesh pattern further enabled fully MRI-compatible imaging without artifacts. Comparing in vivo MRI of the Pt wire and the fully MRI-compatible neural probe verified the acquisition of clear MRI images without artifacts in actual MRI environments. Furthermore, to demonstrate the electrophysiological recording capabilities of the device, in vivo rat experiments targeting the somatosensory area responsive to the hind paw were conducted. The experiments successfully measured the LFP changes upon electrical stimulation of the hind paw. These observations further demonstrated the feasibility of the device as an neural probe through the analysis of LFP changes and power spectral density.

This research suggests that fabrication of neural probes with maximized MRI compatibility is possible when excellent material properties are combined with structural improvements. Such an approach is expected to contribute in solving various issues that arise when devices are exposed to strong EM energy, not only when manufacturing of MRI-compatible neural probes. A current performance limitation of the neural probes is the relatively large size of the open-mesh electrode design, measuring $250\times250~\mu\text{m}^2$. Considering the availability of a small number of channels, these dimensions limit spatial resolution. Thus, advancements in PEDOT:PSS micropatterning technology could allow for the fabrication of smaller-sized electrodes, enabling creation of neural interfaces with broader and more precise measurements.

The convergence of advanced medical imaging capabilities of MRI with neural interfaces that enables handling high-quality biosignals, which are temporally and spatially superior, is challenging. Given the complex structure and mechanisms of the human brain, much of the understanding remains a mystery; while complex multimodal research is necessary. Our study introduces a new direction in the development of electrodes with maximized MRI compatibility, suggesting that it can serve as a powerful tool for various attempts to understand and communicate with the brain, as well as to develop future neural diagnostics.

CRediT authorship contribution statement

Jung-Hoon Hong: Writing - review & editing, Writing - original draft, Visualization, Methodology, Investigation, Formal analysis, Data curation, Conceptualization. Ju Young Lee: Writing – review & editing, Writing - original draft, Visualization, Methodology, Investigation, Formal analysis, Data curation, Conceptualization. Ankan Dutta: Writing - review & editing, Writing - original draft, Visualization, Software, Methodology, Investigation, Formal analysis, Conceptualization. Sol Lip Yoon: Methodology, Data curation, Conceptualization. Young Uk Cho: Methodology, Investigation, Formal analysis, Conceptualization. Kyubeen Kim: Methodology, Formal analysis. Kyowon Kang: Methodology, Formal analysis. Hyun Woo Kim: Methodology, Investigation. Dae-Hee Kim: Methodology. Jaejin Park: Visualization. Myeongki Cho: Methodology. Kiho Kim: Methodology. Jong Bin An: Investigation. Hye-Lan Lee: Methodology, Investigation. Dosik Hwang: Conceptualization. Hyun Jae Kim: Conceptualization. Yoon Ha: Conceptualization. Hye Yeong Lee: Writing – review & editing, Writing - original draft, Project administration, Methodology, Investigation, Data curation, Conceptualization. Huanyu Cheng: Writing review & editing, Writing - original draft, Supervision, Project administration, Funding acquisition, Formal analysis, Data curation, Conceptualization. Ki Jun Yu: Writing - review & editing, Writing - original draft, Supervision, Project administration, Funding acquisition, Formal analysis, Data curation, Conceptualization.

Declaration of competing interest

The authors declare that they have no known competing financial interests or personal relationships that could have appeared to influence the work reported in this paper.

Data availability

Data will be made available on request.

Acknowledgements

This work acknowledges the support received from the National Research Foundation of Korea (Grant Nos. NRF $-\,2021R1A4A1031437,$ RS-2024-00353768). This study was funded by the KIST Institutional Program Project No. 2E31603-22-140 (K.J.Y.). This work was supported by the Yonsei Fellowship, funded by Lee Youn Jae. H.C. acknowledges

the support provided by NIH (Award No. R21EB030140), NSF (Grant No. 2319139), and Penn State University. A.D. acknowledges the support provided by NIH Training Grant T32NS115667 and the Leighton Riess Graduate Fellowship at Penn State University.

Appendix A. Supplementary data

Supplementary data to this article can be found online at https://doi.org/10.1016/j.bios.2024.116446.

References

- Ahn, C.B., Cho, Z.H., 1991. Analysis of the eddy-current induced artifacts and the temporal compensation in nuclear magnetic resonance imaging. IEEE Trans. Med. Imag. 10 (1), 47–52.
- Bhargava, D., Rattanadecho, P., Wessapan, T., 2020. The effect of metal objects on the SAR and temperature increase in the human head exposed to dipole antenna (numerical analysis). Case Stud. Therm. Eng. 22, 100789.
- Bianchi, M., Carli, S., Di Lauro, M., Prato, M., Murgia, M., Fadiga, L., Biscarini, F., 2020. Scaling of capacitance of PEDOT: PSS: volume vs. area. J. Mater. Chem. C 8 (32), 11252–11262.
- Bianchi, M., De Salvo, A., Asplund, M., Carli, S., Di Lauro, M., Schulze-Bonhage, A., Stieglitz, T., Fadiga, L., Biscarini, F., 2022. Poly(3,4-ethylenedioxythiophene)-Based neural interfaces for recording and stimulation: fundamental aspects and in vivo applications. Adv. Sci. 9 (12), e2104701.
- Binan, L., Ajji, A., De Crescenzo, G., Jolicoeur, M., 2014. Approaches for neural tissue regeneration. Stem Cell Rev. Rep. 10 (1), 44–59.
- Carrizales, M., Lake, L.W., 2009. Two-dimensional COMSOL Simulation of Heavy-Oil Recovery by Electromagnetic Heating. COMSOL Conference held, Boston, Massachusetts, USA, pp. 10–13.
- Chen, R., Canales, A., Anikeeva, P., 2017. Neural recording and modulation technologies. Nat. Rev. Mater. 2 (2), 1–16.
- Cho, M., Han, J.K., Suh, J., Kim, J.J., Ryu, J.R., Min, I.S., Sang, M., Lim, S., Kim, T.S., Kim, K., Kang, K., Hwang, K., Kim, K., Hong, E.B., Nam, M.H., Kim, J., Song, Y.M., Lee, G.J., Cho, I.J., Yu, K.J., 2024a. Fully bioresorbable hybrid opto-electronic neural implant system for simultaneous electrophysiological recording and optogenetic stimulation. Nat. Commun. 15 (1), 2000.
- Cho, Y., Park, S., Lee, J., Yu, K.J., 2021. Emerging materials and technologies with applications in flexible neural implants: a comprehensive review of current issues with neural devices. Adv. Mater. 33 (47), e2005786.
- Cho, Y.U., Kim, K., Dutta, A., Park, S.H., Lee, J.Y., Kim, H.W., Park, J., Kim, J., Min, W.K., Won, C., 2024b. MRI-Compatible, transparent PEDOT: PSS neural implants for the alleviation of neuropathic pain with motor cortex stimulation. Adv. Funct. Mater. 34 (6), 2310908.
- Cho, Y.U., Lee, J.Y., Jeong, U.J., Park, S.H., Lim, S.L., Kim, K.Y., Jang, J.W., Park, J.H., Kim, H.W., Shin, H., 2022a. Ultra-low cost, facile fabrication of transparent neural electrode array for electrocorticography with photoelectric artifact-free optogenetics. Adv. Funct. Mater. 32 (10), 2105568.
- Cho, Y.U., Lim, S.L., Hong, J.-H., Yu, K.J., 2022b. Transparent neural implantable devices: a comprehensive review of challenges and progress. npj Flex. Electron. 6 (1), 53.
- Choi, C.T., Konrad, A., 1991. Finite element modeling of the RF heating process. IEEE Trans. Magn. 27 (5), 4227–4230.
- Chou, C.K., Bassen, H., Osepchuk, J., Balzano, Q., Petersen, R., Meltz, M., Cleveland, R., Lin, J.C., Heynick, L., 1996. Radio frequency electromagnetic exposure: tutorial review on experimental dosimetry. Bioelectromagnetics 17 (3), 195–208.
- Chuapoco, M.R., Choy, M., Schmid, F., Duffy, B.A., Lee, H.J., Lee, J.H., 2019. Carbon monofilament electrodes for unit recording and functional MRI in same subjects. Neuroimage 186, 806–816.
- Collins, M.N., Zamboni, F., Serafin, A., Escobar, A., Stepanian, R., Culebras, M., Reis, R. L., Oliveira, J.M., 2022. Emerging scaffold-and cellular-based strategies for brain tissue regeneration and imaging. models 1 (2), 129–150.
- tissue regeneration and imaging. models 1 (2), 129–150.

 Davis, P.L., Crooks, L., Arakawa, M., McRee, R., Kaufman, L., Margulis, A.R., 1981.

 Potential hazards in NMR imaging: heating effects of changing magnetic fields and RF fields on small metallic implants. AJR Am. J. Roentgenol. 137 (4), 857–860.
- Deistung, A., Schweser, F., Reichenbach, J.R., 2017. Overview of quantitative susceptibility mapping. NMR Biomed. 30 (4), e3569.
- Dempsey, M.F., Condon, B., 2001. Thermal injuries associated with MRI. Clin. Radiol. 56 (6), 457–465.
- Djukić, D., Janković, V., Matić, I., Petrović, N., 2006. The IMO Compendium: a Collection of Problems Suggested for the International Mathematical Olympiads: 1959-2004. Springer.
- Erhardt, J.B., Fuhrer, E., Gruschke, O.G., Leupold, J., Wapler, M.C., Hennig, J., Stieglitz, T., Korvink, J.G., 2018. Should patients with brain implants undergo MRI? J. Neural. Eng. 15 (4), 041002.
- Fan, J.A., Yeo, W.H., Su, Y., Hattori, Y., Lee, W., Jung, S.Y., Zhang, Y., Liu, Z., Cheng, H., Falgout, L., Bajema, M., Coleman, T., Gregoire, D., Larsen, R.J., Huang, Y., Rogers, J. A., 2014. Fractal design concepts for stretchable electronics. Nat. Commun. 5 (1), 3266
- Fleisch, D., 2008. A Student's Guide to Maxwell's Equations. Cambridge University Press.

- Foster, K.R., Glaser, R., 2007. Thermal mechanisms of interaction of radiofrequency energy with biological systems with relevance to exposure guidelines. Health. Phys. Met. 92 (6), 609–620.
- Galili, I., Kaplan, D., Lehavi, Y., 2006. Teaching Faraday's law of electromagnetic induction in an introductory physics course. Am. J. Phys. 74 (4), 337–343.
- Graf, H., Steidle, G., Schick, F., 2007. Heating of metallic implants and instruments induced by gradient switching in a 1.5-Tesla whole-body unit. J. Magn. Reson. Imag. 26 (5), 1328–1333.
- Guan, S., Wang, J., Gu, X., Zhao, Y., Hou, R., Fan, H., Zou, L., Gao, L., Du, M., Li, C., Fang, Y., 2019. Elastocapillary self-assembled neurotassels for stable neural activity recordings. Sci. Adv. 5 (3), eaav2842.
- Hidalgo-Tobon, S.S., 2010. Theory of gradient coil design methods for magnetic resonance imaging. Concepts Magn. Reson. 36 (4), 223–242.
- Kang, K., Ye, S., Jeong, C., Jeong, J., Ye, Y.S., Jeong, J.Y., Kim, Y.J., Lim, S., Kim, T.H., Kim, K.Y., Kim, J.U., Kim, G.I., Chun, D.H., Kim, K., Park, J., Hong, J.H., Park, B., Kim, K., Jung, S., Baek, K., Cho, D., Yoo, J., Lee, K., Cheng, H., Min, B.W., Kim, H.J., Jeon, H., Yi, H., Kim, T.I., Yu, K.J., Jung, Y., 2024. Bionic artificial skin with a fully implantable wireless tactile sensory system for wound healing and restoring skin tactile function. Nat. Commun. 15 (1), 10.
- Kennedy, M.W., Akhtar, S., Bakken, J.A., Aune, R.E., 2011. Analytical and experimental validation of electromagnetic simulations using COMSOL®, re inductance, induction heating and magnetic fields. COMSOL users conference, Stuttgart Germany 1–9.
- Lee, J.Y., Park, S.H., Kim, Y., Cho, Y.U., Park, J., Hong, J.-H., Kim, K., Shin, J., Ju, J.E., Min, I.S., 2022. Foldable three dimensional neural electrode arrays for simultaneous brain interfacing of cortical surface and intracortical multilayers. npj Flex. Electron. 6 (1), 86.
- Lottner, T., Reiss, S., Rieger, S.B., Schuettler, M., Fischer, J., Bielak, L., Ozen, A.C., Bock, M., 2022. Radio-frequency induced heating of intra-cranial EEG electrodes: the more the colder? Neuroimage 264, 119691.
- Lu, L., Fu, X., Liew, Y., Zhang, Y., Zhao, S., Xu, Z., Zhao, J., Li, D., Li, Q., Stanley, G.B., Duan, X., 2019. Soft and MRI compatible neural electrodes from carbon nanotube fibers. Nano Lett. 19 (3), 1577–1586.
- Luan, L., Robinson, J.T., Aazhang, B., Chi, T., Yang, K., Li, X., Rathore, H., Singer, A., Yellapantula, S., Fan, Y., Yu, Z., Xie, C., 2020. Recent advances in electrical neural interface engineering: minimal invasiveness, longevity, and scalability. Neuron 108 (2), 302–321.
- Mailly, F., Giani, A., Bonnot, R., Temple-Boyer, P., Pascal-Delannoy, F., Foucaran, A., Boyer, A., 2001. Anemometer with hot platinum thin film. Sens. Actuators, A 94 (1–2). 32–38.
- Moxon, K.A., Hale, L.L., Aguilar, J., Foffani, G., 2008. Responses of infragranular neurons in the rat primary somatosensory cortex to forepaw and hindpaw tactile stimuli. Neuroscience 156 (4), 1083–1092.
- Muranaka, H., Horiguchi, T., Usui, S., Ueda, Y., Nakamura, O., Ikeda, F., 2007.
 Dependence of RF heating on SAR and implant position in a 1.5T MR system. Magn.
 Reson. Med. Sci. 6 (4), 199–209.
- Nyenhuis, J.A., Park, S.-M., Kamondetdacha, R., Amjad, A., Shellock, F.G., Rezai, A.R., 2005. MRI and implanted medical devices: basic interactions with an emphasis on heating. IEEE Trans. Device Mater. Reliab. 5 (3), 467–480.
- Park, J., Kim, K., Kim, Y., Kim, T.S., Min, I.S., Li, B., Cho, Y.U., Lee, C., Lee, J.Y., Gao, Y., Kang, K., Kim, D.H., Choi, W.J., Shin, H.B., Kang, H.K., Song, Y.M., Cheng, H., Cho, I. J., Yu, K.J., 2023. A wireless, solar-powered, optoelectronic system for spatial restriction-free long-term optogenetic neuromodulations. Sci. Adv. 9 (39), eadi8918.
- Pearce Williams, L., 1963. Faraday's discovery of electromagnetic induction. Contemp. Phys. 5 (1), 28–37.
- Salvi, D., Boldor, D., Aita, G., Sabliov, C., 2011. COMSOL Multiphysics model for continuous flow microwave heating of liquids. J. Food Eng. 104 (3), 422–429.
- Sang, M., Kim, K., Shin, J., Yu, K.J., 2022. Ultra-Thin flexible encapsulating materials for soft bio-integrated electronics. Adv. Sci. 9 (30), e2202980.
- Sayed, D., Chakravarthy, K., Amirdelfan, K., Kalia, H., Meacham, K., Shirvalkar, P., Falowski, S., Petersen, E., Hagedorn, J.M., Pope, J., Leever, J., Group, A.M.C.W., Deer, T., 2020. A comprehensive practice guideline for magnetic resonance imaging compatibility in implanted neuromodulation devices. Neuromodulation 23 (7), 893–911
- Seo, K.J., Artoni, P., Qiang, Y., Zhong, Y., Han, X., Shi, Z., Yao, W., Fagiolini, M., Fang, H., 2019. Transparent, flexible, penetrating microelectrode arrays with capabilities of single-unit electrophysiology. Adv. Biosyst. 3 (3), e1800276.
- Seo, Y., Wang, Z.J., 2021. Measurement and evaluation of specific absorption rate and temperature elevation caused by an artificial hip joint during MRI scanning. Sci. Rep. 11 (1), 1134.
- Shabani, L., Abbasi, M., Azarnew, Z., Amani, A.M., Vaez, A., 2023. Neuronanotechnology: diagnostic and therapeutic nano-based strategies in applied neuroscience. Biomed. Eng. Online 22 (1), 1.
- Shen, K., Chen, O., Edmunds, J.L., Piech, D.K., Maharbiz, M.M., 2023. Translational opportunities and challenges of invasive electrodes for neural interfaces. Nat. Biomed. Eng. 7 (4), 424–442.
- Shi, Y., Zhang, C., Li, R., Cai, M., Jia, G., 2015. Theory and application of magnetic flux leakage pipeline detection. Sensors 15 (12), 31036–31055.
- Sophian, A., Tian, G., Taylor, D., Rudlin, J., 2001. Electromagnetic and eddy current NDT: a review. Insight 43 (5), 302–306.
- Starčuková, J., Starčuk Jr, Z., Hubálková, H., Linetskiy, I., 2008. Magnetic susceptibility and electrical conductivity of metallic dental materials and their impact on MR imaging artifacts. Dent. Mater. 24 (6), 715–723.
- Tang, X., Shen, H., Zhao, S., Li, N., Liu, J., 2023. Flexible brain–computer interfaces. Nat. Electron. 6 (2), 109–118.

- Thelen, A., Bauknecht, H.C., Asbach, P., Schrom, T., 2006. Behavior of metal implants used in ENT surgery in 7 Tesla magnetic resonance imaging. Eur. Arch. Oto-Rhino-Laryngol. 263 (10), 900–905.
- Tian, L., Zimmerman, B., Akhtar, A., Yu, K.J., Moore, M., Wu, J., Larsen, R.J., Lee, J.W., Li, J., Liu, Y., 2019. Large-area MRI-compatible epidermal electronic interfaces for prosthetic control and cognitive monitoring. Nat. Biomed. Eng. 3 (3), 194–205.
- Turner, R., 1993. Gradient coil design: a review of methods. Magn. Reson. Imaging 11 (7), 903–920.
- Volkov, A.V., Wijeratne, K., Mitraka, E., Ail, U., Zhao, D., Tybrandt, K., Andreasen, J.W., Berggren, M., Crispin, X., Zozoulenko, I.V., 2017. Understanding the capacitance of PEDOT: PSS. Adv. Funct. Mater. 27 (28), 1700329.
- Winter, L., Seifert, F., Zilberti, L., Murbach, M., Ittermann, B., 2021. MRI-related heating of implants and devices: a review. J. Magn. Reson. Imag. 53 (6), 1646–1665.
- Zhang, Y., Le, S., Li, H., Ji, B., Wang, M.H., Tao, J., Liang, J.Q., Zhang, X.Y., Kang, X.Y., 2021. MRI magnetic compatible electrical neural interface: from materials to application. Biosens. Bioelectron. 194, 113592.

- Zhao, N., Zhu, Z., Liu, W., 2011. Rotor eddy current loss calculation and thermal analysis of permanent magnet motor and generator. IEEE Trans. Magn. 47 (10), 4199–4202.
- Zhao, S., Li, G., Tong, C., Chen, W., Wang, P., Dai, J., Fu, X., Xu, Z., Liu, X., Lu, L., Liang, Z., Duan, X., 2020. Full activation pattern mapping by simultaneous deep brain stimulation and fMRI with graphene fiber electrodes. Nat. Commun. 11 (1), 1788.
- Zhao, S., Liu, X., Xu, Z., Ren, H., Deng, B., Tang, M., Lu, L., Fu, X., Peng, H., Liu, Z., 2016. Graphene encapsulated copper microwires as highly MRI compatible neural electrodes. Nano Lett. 16 (12), 7731–7738.
- Zrinzo, L., Yoshida, F., Hariz, M.I., Thornton, J., Foltynie, T., Yousry, T.A., Limousin, P., 2011. Clinical safety of brain magnetic resonance imaging with implanted deep brain stimulation hardware: large case series and review of the literature. World Neurosurg 76 (1–2), 164–172.; discussion 169-173.

<u>Update</u>

Biosensors and Bioelectronics

Volume 263, Issue, 1 November 2024, Page

DOI: https://doi.org/10.1016/j.bios.2024.116600

FISEVIER

Contents lists available at ScienceDirect

Biosensors and Bioelectronics

journal homepage: www.elsevier.com/locate/bios





Corrigendum to "Monolayer, open-mesh, pristine PEDOT:PSS-based conformal brain implants for fully MRI-compatible neural interfaces" [Biosens. Bioelectron. 260 (2024) 116446]

Jung-Hoon Hong ^{a,1}, Ju Young Lee ^{a,1}, Ankan Dutta ^{b,c,1}, Sol Lip Yoon ^d, Young Uk Cho ^{a,e}, Kyubeen Kim ^a, Kyowon Kang ^a, Hyun Woo Kim ^a, Dae-Hee Kim ^f, Jaejin Park ^a, Myeongki Cho ^a, Kiho Kim ^a, Jong Bin An ^g, Hye-Lan Lee ^d, Dosik Hwang ^h, Hyun Jae Kim ^g, Yoon Ha ^{d,i}, Hye Yeong Lee ^{d,***}, Huanyu Cheng ^{b,c,**}, Ki Jun Yu ^{a,i,j,*}

- ^a Functional Bio-integrated Electronics and Energy Management Lab, School of Electrical and Electronic Engineering, Yonsei University, 50 Yonsei-ro, Seodaemun-gu, 03722, Seoul, Republic of Korea
- b Department of Engineering Science and Mechanics, The Pennsylvania State University, University Park, 16802, State College, PA, USA
- ^c Center for Neural Engineering, The Pennsylvania State University, University Park, 16802, State College, PA, USA
- d Spine & Spinal Cord Institute, Department of Neurosurgery, College of Medicine, Yonsei University, 03722, Seoul, Republic of Korea
- e Center for Emergent Matter Science (CEMS), RIKEN, The Institute of Physical and Chemical Research, 351-0198, Saitama, Japan
- f Avison Biomedical Research Center, College of Medicine, Yonsei University, 50-1 Yonsei-ro, Seodaemun-gu, 03722, Seoul, Republic of Korea
- g Electronic Device Laboratory, School of Electrical and Electronic Engineering, Yonsei University, 50 Yonsei-ro, Seodaemun-gu, 03722, Seoul, Republic of Korea
- ^h School of Electrical and Electronic Engineering, Yonsei University, 50 Yonsei-ro, Seodaemun-gu, 03722, Seoul, Republic of Korea
- i The Biotech Center, Pohang University of Science and Technology (POSTECH), 77 Cheongam-Ro, Nam-Gu, Pohang, Gyeongbuk, 37673, Republic of Korea
- j Department of Electrical and Electronic Engineering, YU-Korea Institute of Science and Technology (KIST) Institute, Yonsei University, 50, Yonsei-ro, Seodaemun-gu, 03722, Seoul, Republic of Korea

The authors regret the corresponding author, Ki Jun Yu's affiliations should be as follows.

Ki Jun Yu ^{a,i,j}*

- a. Functional Bio-integrated Electronics and Energy Management Lab, School of Electrical and Electronic Engineering, Yonsei University, 50 Yonsei-ro, Seodaemun-gu, 03722, Seoul, Republic of Korea
 - i. The Biotech Center, Pohang University of Science and Technology

(POSTECH), 77 Cheongam-Ro, Nam-Gu, Pohang, Gyeongbuk, 37673, Republic of Korea

j. Department of Electrical and Electronic Engineering, YU-Korea Institute of Science and Technology (KIST) Institute, Yonsei University, 50, Yonsei-ro, Seodaemun-gu, 03722, Seoul, Republic of Korea

The authors would like to apologise for any inconvenience caused.

DOI of original article: https://doi.org/10.1016/j.bios.2024.116446.

^{*} Corresponding author. Functional Bio-integrated Electronics and Energy Management Lab, School of Electrical and Electronic Engineering, Yonsei University, 50 Yonsei-ro, Seodaemun-gu, 03722, Seoul, Republic of Korea.

^{**} Corresponding author. Department of Engineering Science and Mechanics, The Pennsylvania State University, University Park, State College, 16802, PA, USA.

^{***} Corresponding author. Spine & Spinal Cord Institute, Department of Neurosurgery, College of Medicine, Yonsei University, 03722, Seoul, Republic of Korea. *E-mail addresses*: kimura416@yuhs.ac (H.Y. Lee), huanyu.cheng@psu.edu (H. Cheng), kijunyu@yonsei.ac.kr (K.J. Yu).

¹ These authors contributed equally to this work.